

# ON THE PENUMBRAL JETLIKE FEATURES AND CHROMOSPHERIC BOW SHOCKS

M. RYUTOVA

Lawrence Livermore National Laboratory/IGPP, Livermore, CA 94550; ryutova1@llnl.gov

AND

T. BERGER, Z. FRANK, AND A. TITLE

Lockheed Martin Solar and Astrophysics Laboratory, Palo Alto, CA 94304; berger@lmsal.com, zoe@lmsal.com, title@lmsal.com

Received 2008 May 28; accepted 2008 July 1

## ABSTRACT

We present observations of sunspot penumbrae obtained during the disk passage of AR 10923 (2006 November 10–20) with the SOT instrument on *Hinode* in 4305 Å G band and Ca II 8500 Å H line. Along with recently discovered jetlike features (Katsukawa et al. 2007), we find other kinds of bright elongated transients abundantly pervading the entire penumbra and drifting as a whole in a direction almost perpendicular to their long axes. Their measured velocities strongly depend on their orientation with respect to the line of sight and range from  $\simeq 1$  to  $\simeq 20$  km s $^{-1}$ . We present quantitative analysis of these features and interpret them relative to our recent penumbral model (Ryutova et al. 2008) to show that they are produced by shocks resulting from a slingshot effect associated with the ongoing reconnection processes in neighboring penumbral filaments. Due to sharp stratification of the low atmosphere, postreconnection flux tubes moving upward quickly accelerate. At transonic velocities a bow (*detached*) shock is formed in front of the flux tube, as usually occurs in cases of blunt bodies moving with supersonic velocities. Observed parameters of transients are in good agreement with calculated parameters of bow shocks. On some, much more rare occasions compared to “drifting” bow-shock-type transients, there appear compact bright transients moving in the radial direction, along their long axis, and having velocities of 20–50 km s $^{-1}$ . We relate these features to a category of true microjets.

*Subject headings:* Sun: chromosphere — Sun: filaments — Sun: magnetic fields — Sun: photosphere — sunspots

## 1. INTRODUCTION

High-cadence observations with the Solar Optical Telescope (SOT) on *Hinode* have led to the discovery of frequent transient brightenings in the penumbral chromospheres with lifetimes of  $\sim 1$  minute (Katsukawa et al. 2007), referred to as penumbral microjets. They are seen in Ca II H line observations in the form of bright strokes abundantly covering the entire penumbra. Their typical length is found to be between 1000 and 4000 km, and some may reach 10,000 km. Their width is  $\sim 400$  km. It was found also that microjets are almost parallel to the penumbral filaments in the radial direction (which makes them difficult to identify when the sunspot is close to disk center) but are more vertical to the surface than penumbral filaments. The estimated elevation angles range from 20° to 60°, but most were found to be between 30° and 50°. Katsukawa et al. (2007) suggested that the observed microjets could be associated with magnetic reconnection in the penumbra. As the physical nature of these phenomena at the time of their discovery was not clear, the authors left room for two possible but different explanations:

1. One is that “the jetlike brightenings are a signature of plasma transiently heated to much higher temperatures.”
2. The other is that transients represent true mass motion with supersonic velocities, i.e., microjets.

In this paper we show that both explanations are true and are related to two different classes of events. One class includes bright elongated transients drifting as a whole in a direction almost perpendicular to their long axes. Their properties are well represented by bow shocks, and we classify them as bow-shock-type transients. The other class includes compact, short-lived,

and much faster bright transients exhibiting true plasma motion “along” their axes. We classify these events as microjets. The triggering mechanism for either kind of transient is indeed the reconnection between the neighboring penumbral filaments, but it is the postreconnection processes and local physical conditions that determine their specific nature.

We use the observations of sunspot penumbrae obtained during the disk passage of AR 10923 (2006 November 10–20) with the SOT instrument in 4305 Å G band and Ca II 8500 Å H line. Movies taken at 8 s cadence, showing various positions of the sunspot as it passes disk center from limb to limb, reveal more details in properties of jetlike phenomena. These observations confirm the above statement and clearly show the existence of two classes of phenomena: (1) a large number of elongated transient brightenings drifting as a whole in a direction almost perpendicular to their long axes; their lifetimes are between  $\simeq 40$  s and  $\simeq 6$  minutes; and (2) a small number of true plasma streaming, microjets, with velocities  $\geq 20$  km s $^{-1}$ , with lifetimes always  $\leq 1$  minute.

In line with a previous paper on the fine structure and dynamics of sunspot penumbrae (Ryutova et al. 2008), we address the origin and physical nature of the observed transients. We find that their appearance is a natural consequence of ongoing reconnection processes among penumbral filaments. Special conditions of the photospheric reconnection and postreconnection processes determine how penumbral filaments evolve, how they affect the overlying atmosphere, and what their observable signatures are in the chromosphere.

In § 2 we briefly describe the observed properties of penumbrae and basic elements of our model. We show that plasma jets and transient brightenings must be expected as a natural consequence of the ongoing and ubiquitous reconnection processes

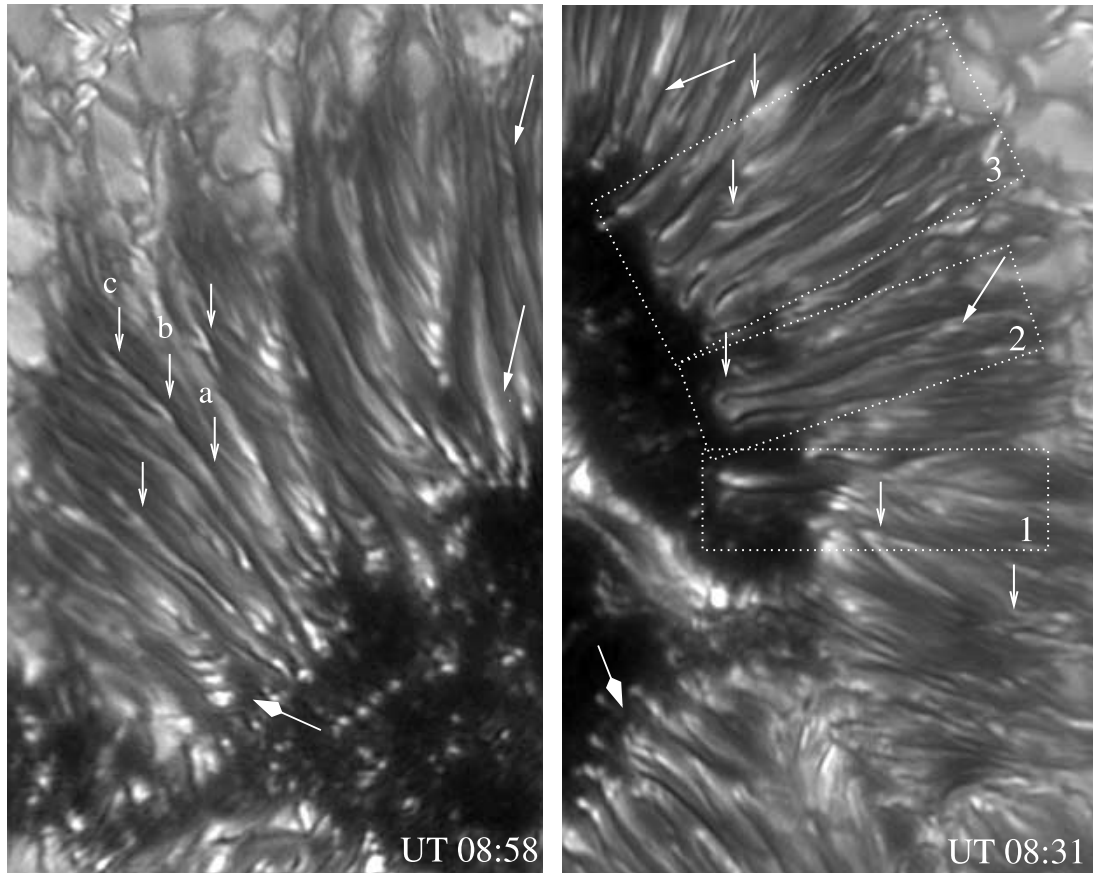


FIG. 1.—Eastward and westward parts of a sunspot showing various structures in penumbral filaments taken with the SST on La Palma (2006 June 6). Small downward-pointing arrows show apparent “splitting” of filaments. Note an enhanced brightening in all the branching points. Three arrows marked by “a,” “b,” and “c” show multiple branching of one filament. Although the snapshot caught them together, the branchings occurred at different times. The thick arrow in the left panel shows a series of intense bright points, and in the right panel, a multiwire view of filaments. The westward part of the penumbra (*right*) is on the disk center side and therefore shows more dark-cored filaments than the eastward part of the penumbra (Sütterlin et al. 2004). The dotted boxes are explained below. From Ryutova et al. (2008).

among flux tubes comprising penumbrae. In § 3 we present results of observations. In § 4 we discuss the mechanisms that may explain the observed properties of the elongated brightenings as bow shocks, formed in front of reconnected flux tubes moving upward with supersonic velocities. We then specify conditions when, instead of the creation of bow shocks, a collimation of flows occurs, leading to the formation of true microjets. Section 5 contains a brief summary of our results.

## 2. PROPERTIES OF PENUMBRAE AND BASIC ELEMENTS OF THE MODEL

High-resolution observations with the Swedish 1 m Solar Telescope (SST) on La Palma revealed the fine substructure of penumbral filaments and new properties of their dynamics (Scharmer et al. 2002; Berger et al. 2004; Bellot Rubio et al. 2004, 2005; Borrero et al. 2004; Ryutova et al. 2008). These findings provide both the basis and constraints for models of the penumbra. These models not only must explain the properties of individual filaments but should also shed light on the formation of penumbrae per se. Key observational findings are illustrated in Figure 1 and can briefly be summarized as follows: (1) Most filaments in 4305 Å G band and 24368 continuum lines consist of a dark core surrounded by bright “walls” (first reported by Scharmer et al. 2002). (2) They are adjacent to bright points that may be found anywhere along their length, often inside umbrae (Scharmer et al. 2002; Rouppe van der Voort et al. 2004; Ryutova et al. 2008). (3) Filaments with or without dark cores may branch into several

filaments anywhere in the penumbra. A branching region is always brighter than the filament itself (Sütterlin et al. 2004; Bellot Rubio et al. 2005; Ryutova et al. 2008). (4) Many filaments exhibit twist along their lengths, resembling cylindrical helices having various pitches (Scharmer et al. 2002; Ryutova et al. 2008). (5) The average lifetime of individual filaments is 1–2 hr. (6) Several filaments may twist around each other into a bunch, resembling multiwire cable. When unwinding, the individual filaments often keep their identity, but the process itself is accompanied by localized sporadic brightenings (Ryutova et al. 2008; Borrero et al. 2008). (7) The inclination of the dark-cored filaments with respect to the normal varies from  $35^\circ$  in the inner penumbra to about  $60^\circ$  toward the outer penumbra (Langhans et al. 2005). (8) The line of sight and transverse magnetic signals are lower in the dark (cooler) cores than in the lateral (warmer) brightenings (Langhans et al. 2005; Bellot Rubio et al. 2005, 2007; van Noort & Rouppe van der Voort 2008). (9) The ratio of filament radius and pitch is about the same for the majority of the filaments (Ryutova et al. 2008).

We emphasize that the formation mechanism of the penumbra should also explain the listed properties of individual filaments. Moreover, this mechanism must be part of the physical process that determines the impact of penumbral dynamics on the overlying atmosphere and its observed signatures. We demonstrate that the mechanism proposed recently by Ryutova et al. (2008) satisfies these conditions. The mechanism is based on the well-established assumption that the umbra itself is a dense conglomerate of noncollinear interlaced flux tubes.

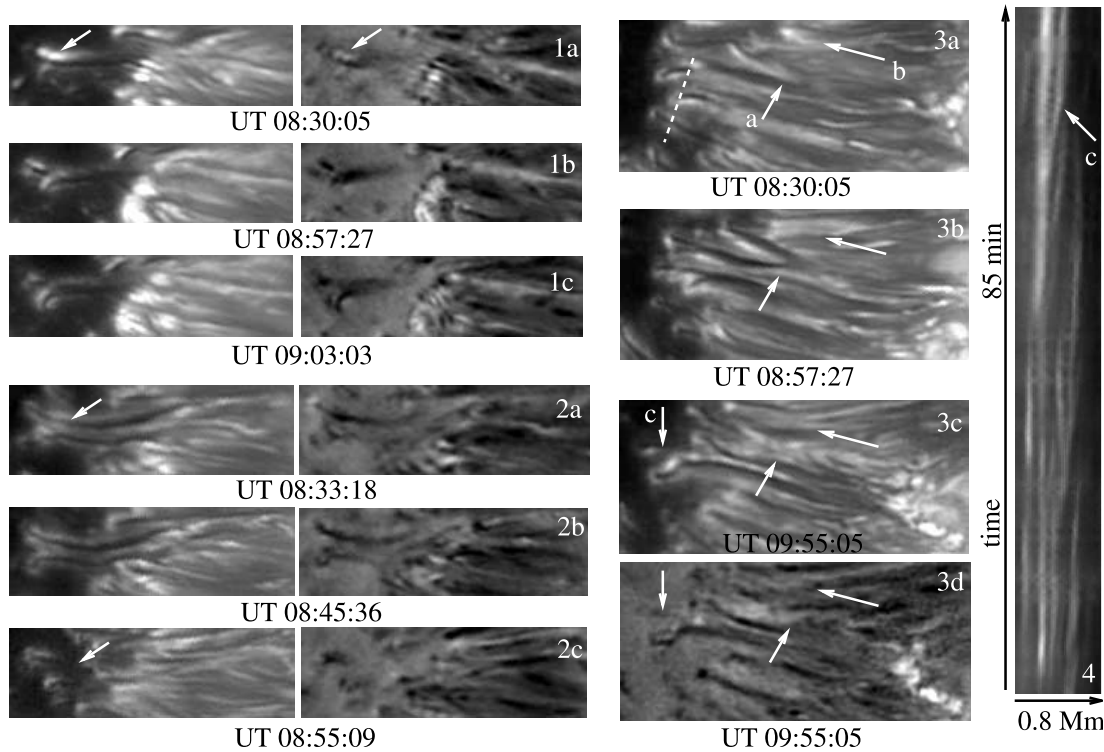


FIG. 2.— Examples of reconnecting filaments in three instances of time. Boxes 1–3 correspond to areas marked by dotted boxes in Fig. 1. The upper six panels marked by (1a)–(1c) show simultaneous G-band and G-band/continuum difference images of two neighboring filaments; initially the longer filament overlays the shorter one. In subsequent instances, it seems that the filaments have exchanged their left ends. The lower six panels marked by (2a)–(2c) show another example of filaments in a later stage of their interaction. In both cases the interaction is accompanied by the enhanced brightening (marked by white arrows). Panels (3a)–(3d) show the evolution of a system of filaments. Arrows “a” and “b” show the regions where filaments possibly reconnect and acquire a twisted shape. The dotted line in panel (3a) shows a cut passing through several filaments. A corresponding spacetime image (panel [4]) shows several splitting events and the major “survival,” the filament strongly protruding into the umbra, marked by arrow “c” in panels (3c) and (4). This event is shown simultaneously in G-band and G-band/continuum difference images at UT 09:55:05.

Observations of filamentary structure of umbrae go back to the 1950s, leading to studies of umbral fine structures long before the recent high-resolution observations became available. For example, Papathanasoglou (1971) showed that widths of umbral filaments are  $<1''$ , and dark spacing between them is about  $0.6''$ . Livingston (1991), comparing images of sunspots with different exposures, came to the conclusion that the sunspot umbra also has a filamentary structure and may exhibit the presence of vertical, diverging, and horizontal filaments. Such random alternation of magnetic fluxes and almost nonmagnetic spacing between them are indicative that the umbrae consist of a dense conglomerate of noncollinear flux tubes that are in constant motion relative to one another.

Among fundamental processes in such a conglomerate are reconnection and postreconnection processes. More importantly, in the photosphere and subphotosphere, these processes are radically different from the well-studied case of the low- $\beta$  corona where reconnection liberates a large amount of magnetic energy and results in an in situ heating. In the low atmosphere reconnection does not give an immediate gain in energy, but it puts the system in a strongly nonlinear state (Tarbell et al. 1999; Ryutova et al. 2003).

The most pervasive kind of interaction seen in the observations is indeed the apparent splitting of filaments, accompanied by an enhanced brightening of a small, localized region. This process is ubiquitous and is observed all over the penumbra at any moment of time. Several examples are shown in Figure 2, where three regions, marked by dotted boxes in the right panel of Figure 1, are shown at three instances of time. Panels (1a)–(1c) and (2a)–(2c) of Figure 2 are simultaneous G-band and G-band/continuum dif-

ference images of two different couples of interacting filaments. At UT 08:30:05 an enhanced brightening is quite prominent in the small region marked by arrows. This region becomes the place where left parts of two filaments “exchange” their places, suggesting by its nature a reconnection of filaments (Ryutova et al. 2008). A similar process occurs between the “second couple” shown in panels (2a)–(2c) of Figure 2.

Panels (3a)–(3d) of Figure 2 show complex behavior of filaments as a dense conglomerate. We highlight here two splitting processes marked by short arrow “a” and longer arrow “b.” In both cases after splitting, filaments acquire a twisted shape. In case “a” splitting is seen in both G-band and difference images, while in case “b” splitting is noticeable only in the difference image. The dashed line in panel (3a) of Figure 2 is the cut passing through several dark-cored filaments. The corresponding spacetime image (panel [4] of Fig. 2) shows several splitting events during the time of observation and the major “survival”: the filament strongly protruding into the umbra, marked by arrow “c” in panels (3c) and (4) of Figure 2. Note that, although the snapshot caught these three branching together, they did not appear simultaneously, indicating that the interaction of the filament with different neighbors occurred at different times.

A specific character of postreconnection dynamics at the photospheric level is determined basically by a finite plasma beta and sharp stratification of the low atmosphere. Indeed, the very existence of flux tubes, being in pressure equilibrium with almost nonmagnetic surrounding gaps, i.e.,  $p_{\text{ext}} = p_{\text{in}} + B_{\text{in}}^2/8\pi$ , implies that plasma beta outside the flux tube is greater than unity,  $\beta = 8\pi p_{\text{ext}}/B_{\text{ext}}^2 \gg 1$ , and the parameter  $\beta = 8\pi p_{\text{ext}}/B_{\text{in}}^2 \geq 1$ . Thus, the magnetic energy is less than the gas kinetic energy, but after

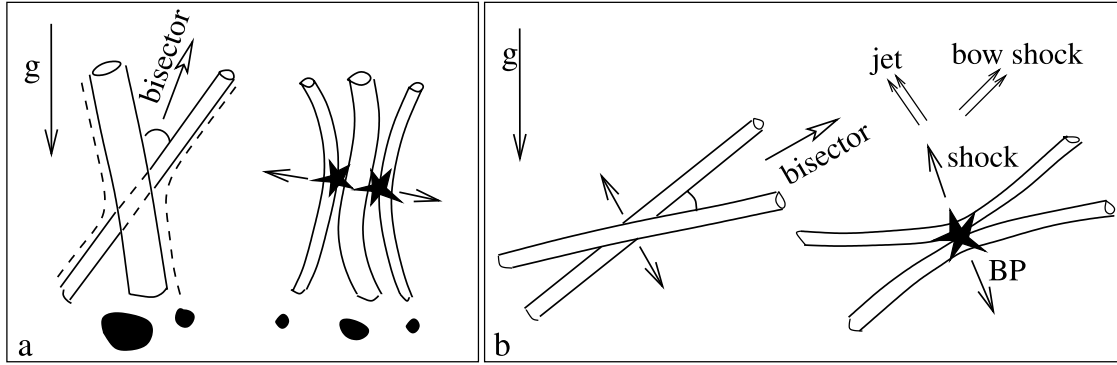


FIG. 3.—Photospheric reconnections between the same polarity flux tubes in sunspot area: (a) reconnection in the central part of the sunspot leading to a fragmentation process; the bisector of the collision angle is close to the line of sight; (b) reconnection between the peripheral filaments when the bisector of the collision angle strongly deviates from the vertical; in this case the upper slingshot generates shocks that eventually lead to the appearance of either plasma jets or bow shocks; an inevitable bright point (BP) in the reconnection region always shows up.

reconnection, magnetic field lines remain confined in thin flux tubes, now curved in shape. In straightening, the reconnection products create a slingshot effect that generates waves. Propagating upward against gravity, these waves quickly become shocks and accelerate further due to the sharp stratification in the low atmosphere.

The dynamics of postreconnection products and their impact on the overlying atmosphere strongly depend on the orientation of filaments and, more importantly, on the inclination of the bisector of their collision angle (Fig. 3).

If the bisector of the collision angle is close to the line of sight, which corresponds mostly to the central part of the sunspot, reconnection between the flux tubes leads to further fragmentation and displacement of reconnection products (Fig. 3a). Gravitational force in this case does not play an essential role in the motion of the reconnection products.

Toward the periphery, flux tubes deviate more and more from the vertical, as does the bisector of their collision angle (Fig. 3b). In this case, along the magnetic tension the reconnection products experience a buoyancy force. In the upper part of the U-shaped form, the magnetic tension and buoyancy force are acting in the same direction, leading to shock formation and the eventual appearance of lateral jets (Tarbell et al. 1999; Ryutova et al. 2003) or the occurrence of bow shocks. In either case the process is accompanied by the enhanced brightening of a small reconnection region and the appearance of a bright point.

It is important that only a limited portion of the flux participates in each elemental act of reconnection. The effective radius is determined by the flux tube parameters and magnetic Reynolds number,  $\text{Re}_m = Lv_A/D_m$ , where  $L$  is the length of the flux tube participating in the reconnection process,  $v_A$  is the Alfvén velocity, and  $D_m$  is a magnetic diffusivity. The maximum rate in the fast reconnection process (Petschek 1964; see also Parker 1979) is estimated as  $w_{\text{max}} \simeq v_A/(\ln \text{Re}_m)$ . The reconnection time over radius  $R$  is therefore

$$\tau_{\text{rec}} \simeq \frac{R}{w_{\text{max}}} = \frac{R \ln \text{Re}_m}{v_A}. \quad (1)$$

For the flux tube to participate in the reconnection process over the length  $L$  (and be able to produce a slingshot effect), the reconnection time,  $\tau_{\text{rec}}$ , must be less than the Alfvén transit time,  $\tau_A = L/2v_A$ . This condition sets the limit on the flux tube radius,  $R_{\text{max}}$ , at which the flux tube participates in an elemental act of reconnection,  $R_{\text{max}} < L/2 \ln \text{Re}_m$ .

For photospheric conditions the Reynolds number is  $\text{Re}_m \simeq 10^3\text{--}10^6$  and a typical length is  $L \simeq 10^3$  km, which gives

$R_{\text{max}} \sim 36\text{--}70$  km. This means that magnetic flux tubes with radii as small as 150–200 km are subject to multiple reconnections (Ryutova et al. 2001, 2003; Tarbell et al. 2000). One therefore must expect that the sunspot, from its central part to periphery, is subject to ongoing reconnection processes.

### 3. OBSERVATIONS WITH SOT ON *Hinode*

We use observations of sunspot penumbrae obtained during the disk passage of AR 10923 (2006 November 10–20) with the SOT instrument on *Hinode* in 4305 Å G band and Ca II 8500 Å line. On most days the SOT correlation tracker worked well and the spacecraft was tracking for the November 10–17 flat-fielded data so the Ca II H images were co-aligned. However, the correlation tracker was not always positioned well for tracking at the limb. In those cases, we used a rigid alignment and drift removal algorithm based on cross correlation over a sequence of images. The accuracy of alignment from frame to frame is within a pixel.

Figure 4 shows the studied sunspot on 2006 November 10 located at a heliospheric angle of  $55^\circ$  toward the east side of disk center. At any moment in time, the penumbra is covered by bright strokes, elongated transients, that last from 30 s to several minutes. Their appearance always correlates with the appearance of bright points in the corresponding G-band image. Some examples are marked by white arrows in Figure 4. White boxes demarcate two regions whose time sequences are shown in Figures 5 and 6. Transients marked by broken arrows are in the decay phase, while their “parental” bright points in G band are still prominent.

Figure 5 shows evolution of three prominent transients during a 4 minute 30 s period. The first frame at UT 13:13:36 shows when transient 1 has just appeared. Transient 2 appeared 30 s earlier. Transient 3 is seen here during its entire lifetime (UT 13:15:06–13:16:37). Note that all three transients are quite similar. They have the same position angle in the plane of the sky. Their intensity increases in time and then either gradually decreases (as in cases 1 and 2) or vanishes abruptly, as in case 3. Lifetimes are  $\geq 6$  minutes (transient 1), 2 minutes (transient 2), and 90 s (transient 3). All three transients seem to be almost motionless. In fact, they are slowly drifting in the direction perpendicular to their long axes, with velocities  $v_1 = 0.6 \text{ km s}^{-1}$ ,  $v_2 = -1.3 \text{ km s}^{-1}$  (a minus sign formally means that, unlike the other two transients, transient 2 is drifting “downward”), and  $v_3 = 3.3 \text{ km s}^{-1}$ . Indices correspond to prescribed numbers. We believe, however, that this is a visual effect associated with the angle between the line of sight and the direction of motion of the transients and that the true velocities of transients are considerably higher. These three examples represent the vast majority of

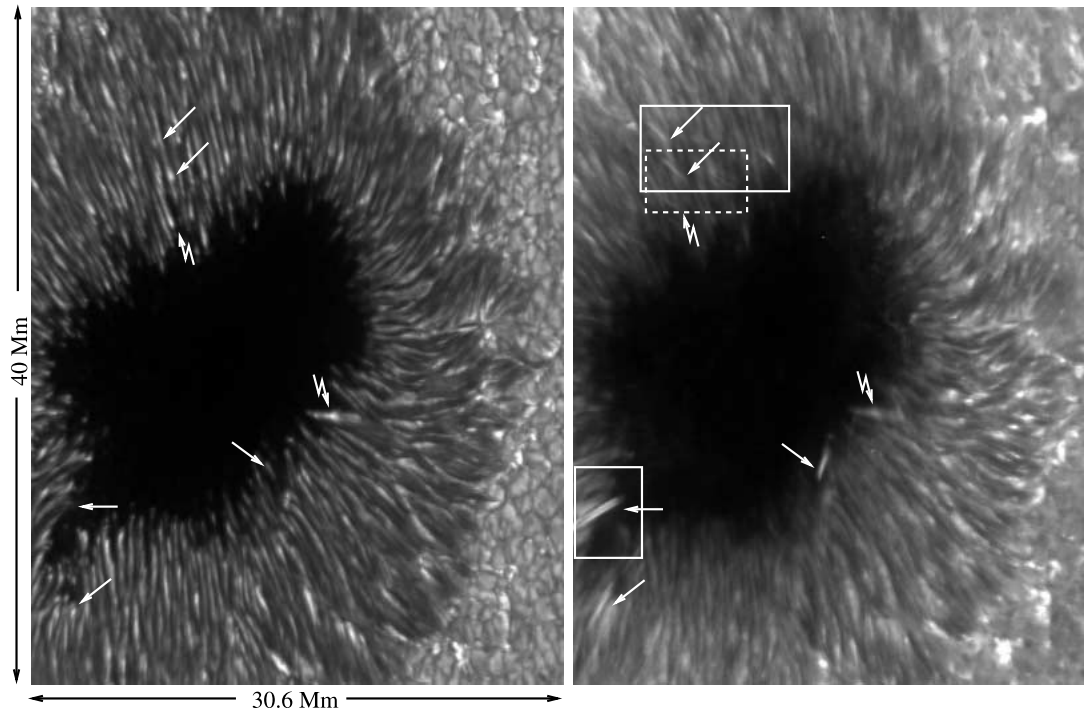


FIG. 4.— Snapshots of the studied region. *Left*: G-band filtergram. *Right*: Ca II  $\lambda 8500$  H line. Usually, transients (seen in the Ca II H line) are closely related to bright points seen in the G-band image (some are marked by arrows). Transients marked by broken arrows are decaying, while their “parental” bright points in G band are still prominent. White boxes demarcate regions shown in Figs. 5, 6, and 7 at several instances in time. Note that the event shown in Fig. 6 occurred about 45 minutes earlier, and its area is marked by a dashed box.

the transient brightenings that always move as a whole in the direction perpendicular to their long axes. Their visual velocities range, in fact, from  $\leq 1$  to  $20 \text{ km s}^{-1}$ .

Another set of slowly drifting transients is shown in Figure 6. We focus on two of them marked as 1 and 2 in a middle frame (UT 12:38:05). The lifetime of both transients is about 5 minutes. The black dashed arrow in the bottom left panel shows the spacetime cut, a procedure that allows us to follow motions of bright and dark patches lying along the cut. The corresponding

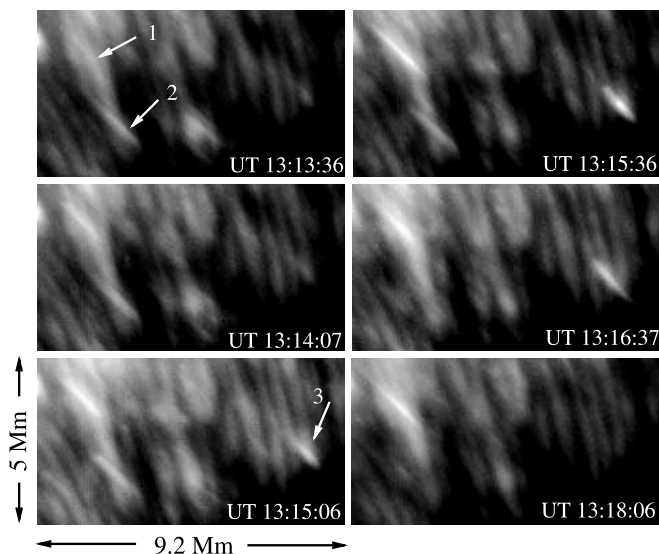


FIG. 5.— Examples of three transients, from the upper white box in Fig. 4, slowly drifting in a direction perpendicular to their long axes. We identify this type of transient as bow shock.

spacetime image is shown in the vertical panel. The cut is made from top to bottom, which, together with the vertical panel, indicates that transients are moving downward. Measured velocities are  $v_1 = 3.9 \text{ km s}^{-1}$  and  $v_2 = 3.1 \text{ km s}^{-1}$ .

A remarkable new feature revealed in these images is that transient 1 has a double structure. This structure starts to develop soon after the transient has appeared (i.e., just 30 s after its “first light”) and, in this particular example, is easily visible during the maximum state of the transients. This important feature turned out to be quite pervasive: many elongated transients show a double structure and patterns similar to those seen in Figure 6. The fact that not all transients show a double structure is due to

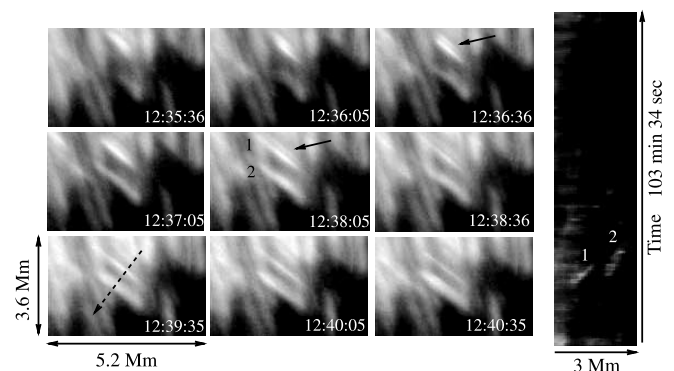


FIG. 6.— Another set of slowly drifting transients. The black dashed arrow in the bottom left panel shows the path along which a spacetime cut is made. The vertical panel is the corresponding spacetime image that allows detection and measurement of the motion of bright and dark patches lying along the cut. We find velocities in the direction of the cut to be  $v_1 = 3.9 \text{ km s}^{-1}$  and  $v_2 = 3.1 \text{ km s}^{-1}$ . Black solid arrows show a new feature found in these observations: the double structure of chromospheric transients.

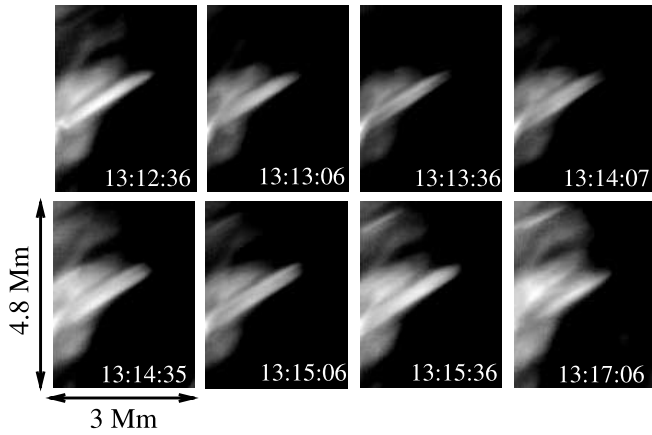


FIG. 7.—Double structure of the elongated transient drifting with velocity  $\sim 1.5 \text{ km s}^{-1}$ . Its true motion, if measured in its trajectory plane, may well be supersonic.

an arbitrary orientation of the plane of transient motion with respect to the line of sight. The same thing affects measured velocities of transients.

Another example of transients exhibiting double structure and the same pattern as above is shown in Figure 7. One can see that this transient at about UT 13:13:36 develops a clearly visible double structure and remains oriented in such a way that its double structure is seen during most of its lifetime ( $\geq 5$  minutes). The transient is drifting from top left to bottom right with velocity  $\sim 1.5 \text{ km s}^{-1}$ . As already emphasized, this velocity, restricted by two-dimensional viewing, strongly depends on the orientation of the plane of motion. In three dimensions the transient may move either toward or away from a viewer. We believe that double structure is a basic property of “drifting”

transients and may have a natural explanation in the frame of our model. Before we discuss details of the model, we look into the properties of chromospheric transients when sunspots move toward the disk center and the west limb.

As already mentioned (Katsukawa et al. 2007), the elongated chromospheric transients in radial directions almost coincide with underlying penumbral filaments and are barely detectable. On some occasions, however, if the transient exhibits proper motion, it can be observed. An example is shown in Figure 8.

The same sunspot, AR 10923, is shown on 2006 November 14, close to disk center. Shown are a G-band and magnetogram image of the sunspot. Ca II H images do not give much information about elongated transients, but an example of a tiny microjet with proper motion is shown in a Ca II H line image. It originates at the base of the fork (marked by black arrows in the upper images) and first appears as an enhanced brightening in the Ca II H line at about UT 10:22:34 (*bottom left panel*). It slowly accelerates and moves during the first 5 minutes with an average velocity  $\simeq 9 \text{ km s}^{-1}$ . Starting from UT 10:27:55, it quickly accelerates, reaching a velocity of  $\simeq 30 \text{ km s}^{-1}$ , and then suddenly disappears. This is one of the examples of collimated plasma streaming that can be classified as a true microjet. Generation of collimated plasma flows requires special conditions (Tarbell et al. 1999; Ryutova et al. 2003). The key element is associated with the geometry of a shock profile and environmental magnetic fields, which may provide conditions for self-focusing of the shock and generation of microjets.

As the sunspot moves toward the limb, the transients become clearly visible and appear elevated with respect to penumbral filaments with angles ranging from  $30^\circ$  to  $50^\circ$ . Figure 9 shows the same sunspot (approaching the west limb) at two heliographic locations:  $42^\circ$  west,  $6^\circ$  south on 2006 November 17 (*left panel*) and  $85^\circ$  west,  $6^\circ$  south on 2006 November 20 (*right panel*). White arrows imitate the azimuthal direction of some transients, showing

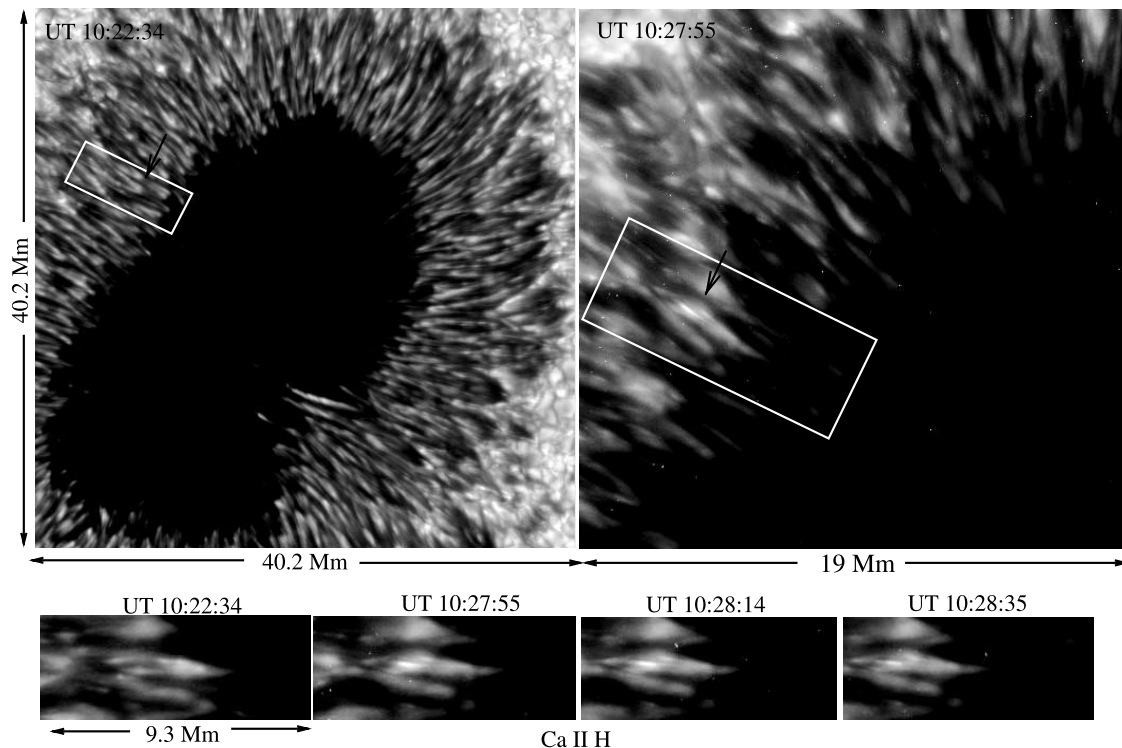


FIG. 8.—Same sunspot, AR 10923, near the disk center. Shown are a G-band image of the sunspot and the enlarged Ca II H image of its upper east quarter. The birth and evolution of a supersonic microjet are shown in Ca II H images at four instances of time. The microjet originated at the base of a fork made by penumbral filaments (marked by black arrows). Its average velocity during the first 5 minutes is  $\simeq 9 \text{ km s}^{-1}$ , reaching  $\simeq 30 \text{ km s}^{-1}$  during the last minute.

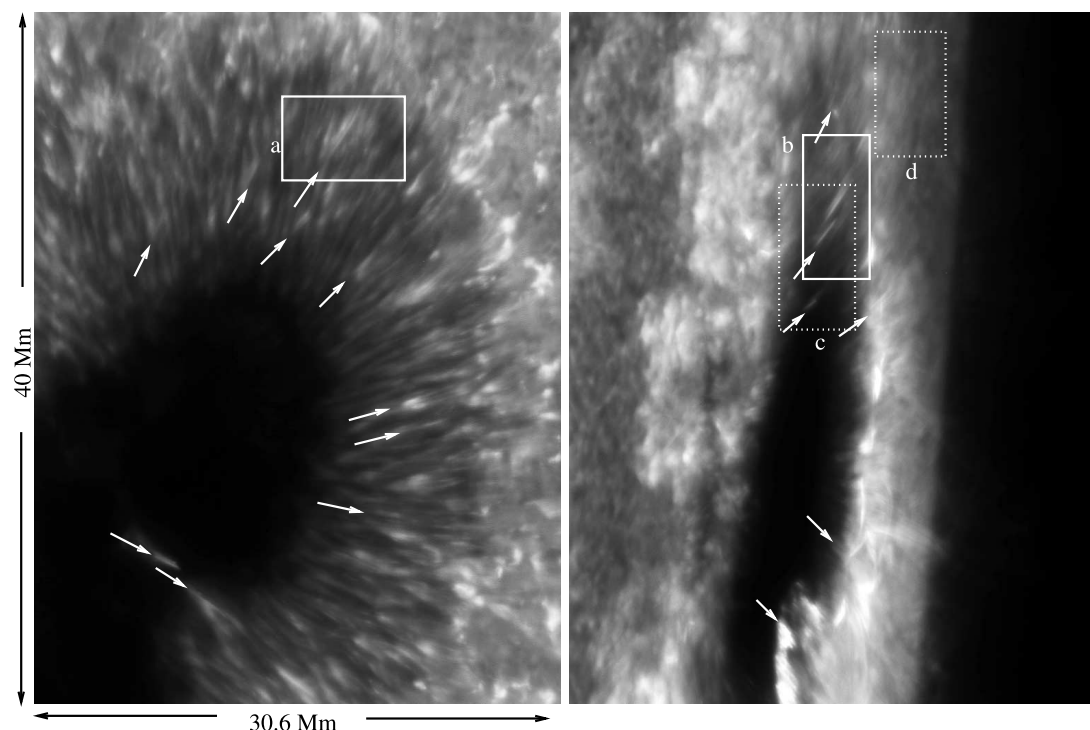


FIG. 9.—Sunspot at two western hemisphere locations: 42° west, 6° south on 2006 November 17 (*left*) and 85° west, 6° south on 2006 November 20 (*right*). White arrows imitate a position angle of some transients showing their fanlike distribution in the plane of the sky. White boxes “a,” “b,” “c,” and “d” demarcate regions shown in subsequent figures.

their fanlike distribution with quite regular position angles. All of the marked examples belong to bow-shock-type transients drifting as a whole in a direction perpendicular to their long axes. As already mentioned, the overwhelming majority of bright transients seen at any given instance of time belong to this class of events. On some occasions there appear true “microjets,” collimated plasma streaming. White boxes in Figure 9 are drawn in solid and dotted lines to denote that the events shown in these boxes occur at different times. Solid boxes mark events occurring around the same time as snapshots of large images shown in Figure 9. Dotted boxes contain events that occur about an hour later.

Figure 10 shows the evolution of two transients during about a 3 minute period. The area with these events is demarcated by a solid box “a” in the snapshot of 2006 November 17. The transient marked by a black arrow is oriented in quite a favorable way to show the formation of a double structure. This is a very typical process that starts with an enhanced brightening already having an elongated form. Soon after formation, the double structure gets quickly stretched until the dissipation process turns on.

This example is a good illustration of the process associated with the postreconnection flux tube moving upward with supersonic velocity. Note that the flux tube, still being cold inside, is

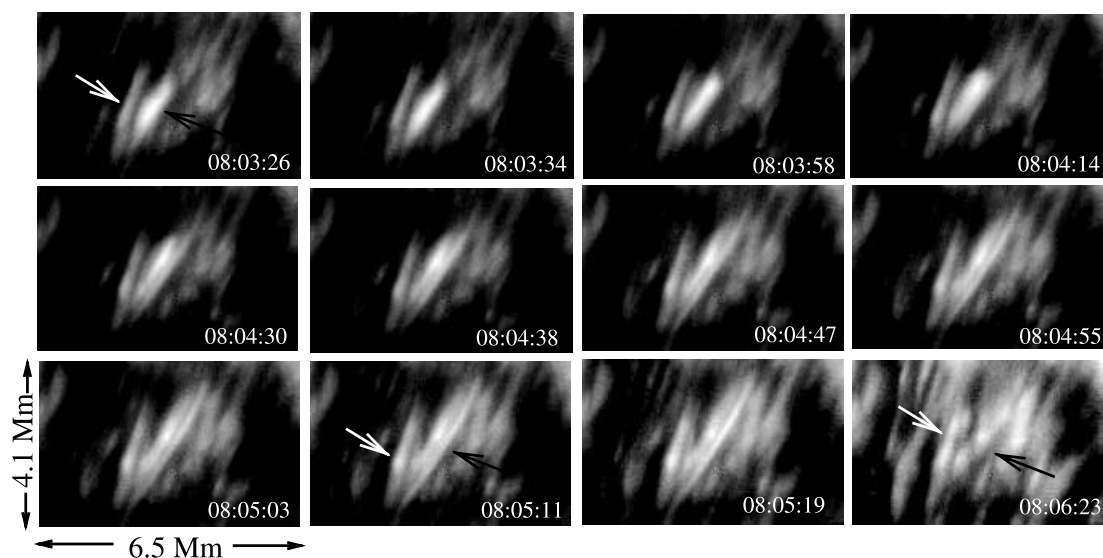


FIG. 10.—Formation and evolution of a bow shock.



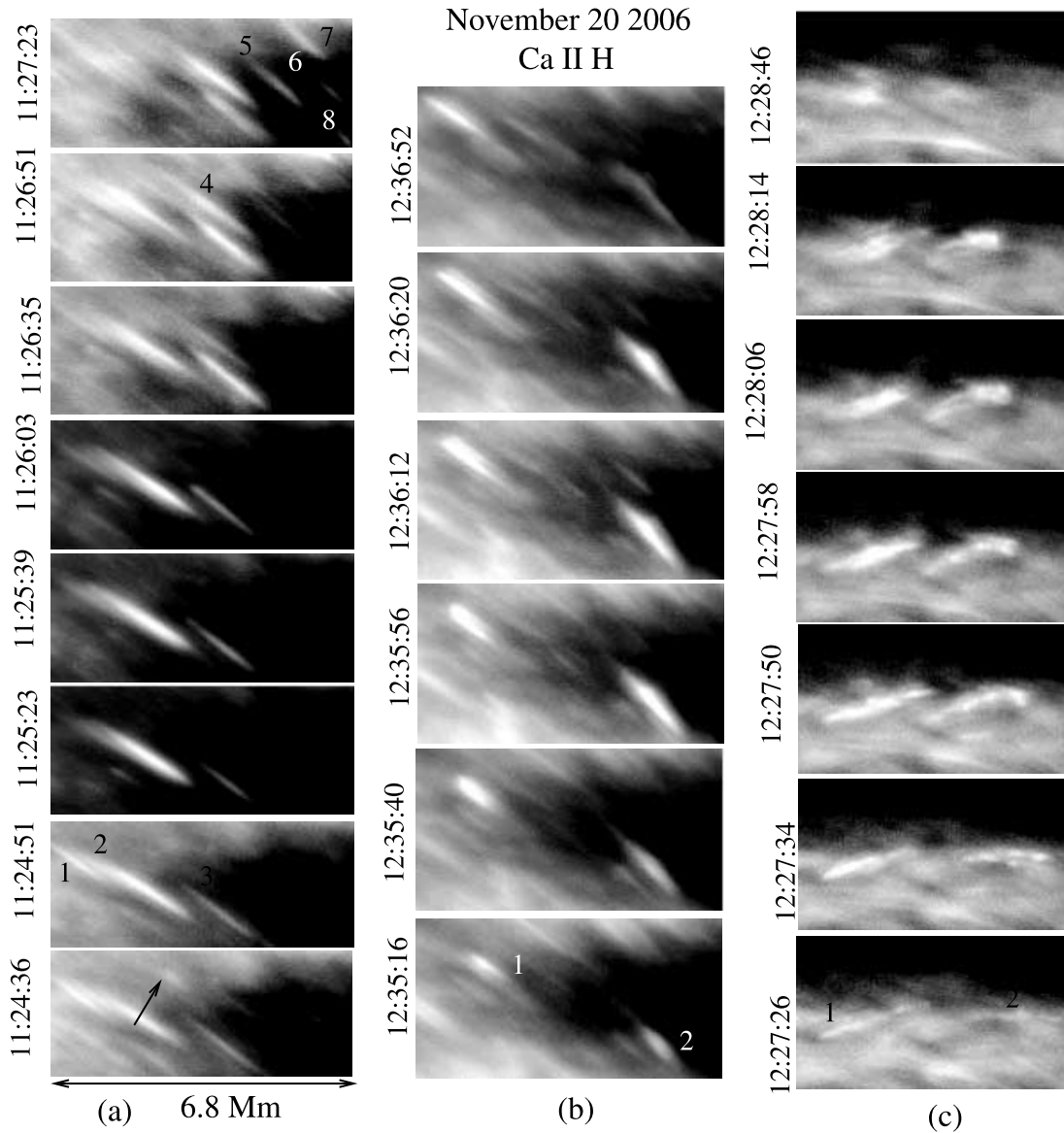


FIG. 11.—Examples of three bright transients under different viewing angles. See text for details.

not visible in Ca II H, but the shock, generated by a slingshot effect resulting from its straightening, heats the plasma. This is a regular occurrence of behind shock heating, which appears as a “first light,” and should manifest itself in a way similar to that shown in the top left panel, including its elongated form (UT 08:03:26).

It is important to note that the flux tube is still a “body” that continues to travel with supersonic velocity. As such, it creates a bow shock in front of it. Indeed, soon after the appearance of the first behind shock brightening, the double structure starts to form and becomes visible at UT 08:04:14. In this particular case, the bow shock appears in about 48 s after the behind shock brightening. As the original shock propagates faster than the flux tube, the bow shock always appears after the regular behind shock heating. This pattern, with various “time delays,” is confirmed in all the observed cases of double structures. We return to this process in the next section and present quantitative estimates.

Note that a standoff distance is clearly visible during the entire evolution of the bow shock until the whole structure starts to dissipate. The velocity of the structure in the plane at a given orientation is  $5.6 \text{ km s}^{-1}$  (directed from top left to bottom right). We believe, however, that the true velocity of the transient is

transonic. If the measured velocity of a transient is  $v_{\text{obs}}$ , then its true velocity can be estimated as  $v \simeq v_{\text{obs}}/\sin \theta$ , where  $\theta$  is an angle between the line of sight and the trajectory plane of the transient. For example, if angle  $\theta = 20^\circ\text{--}40^\circ$ ,  $v \simeq 16.4\text{--}10.1 \text{ km s}^{-1}$ . Another transient in Figure 10, marked by a white arrow, shows only its “thermal” evolution and slow drift with velocity  $1.5 \text{ km s}^{-1}$ . The velocity component of the apparent motion of the transient in the plane of the sky is only  $2.24 \text{ km s}^{-1}$ . To be supersonic, the angle between the plane of motion and line of sight should be  $\leq 16^\circ$ . Nothing contradicts such an orientation; the plane may be parallel to the line of sight, in which case the transient will appear motionless and will only exhibit its “thermal” evolution. We believe that this case is true for the majority of bow-shock-type transients. Given their abundance, quite a large number of transients, however, have a favorable orientation to show their double structure.

Some other examples of transients differently orientated and having thus different velocities are shown in Figure 11. These were taken on 2006 November 20. The first column (the area marked by a solid white box “b” in Fig. 9) shows the most typical picture of several transients (marked 1–8), appearing, evolving, and



disappearing in time intervals less than 3 minutes. In this orientation none of the transients show a double structure and the highest drift velocity measured (transient 2) is  $4.2 \text{ km s}^{-1}$ . This time series shows transient 2 during its entire life ( $\approx 2 \text{ minutes } 15 \text{ s}$ ). At UT 11:24:51, transient 1 is in its final stage. Transient 3, which seems practically motionless, shows its thermal evolution, reaching maximum brightness at UT 11:26:51. From this moment on, it quickly dissipates energy and disappears. Its lifetime is about 3 minutes. At the end of this time sequence (UT 11:26:51) a strong transient appears (transient 4), which quickly gains energy and disappears in 2 minutes. About this time (UT 11:27:23), in the small area of a given frame, four new transients appear almost simultaneously, showing a typical abundance of “one type” of transients.

The central column (the area marked by dotted white box “c” in Fig. 9) shows evolution of two fast “conveniently” oriented transients. In other words, their orientation is such that their measured velocities are supersonic,  $v_1 = 16.8 \text{ km s}^{-1}$  (transient 1) and  $v_2 = 8.8 \text{ km s}^{-1}$  (transient 2), and a double structure of transient 1 can be seen.

The right column (the area marked by dotted white box “d” in Fig. 9, located on the farther side of the penumbra, unlike previous areas) shows the evolution of two other supersonic transients. Their measured velocities exceed  $v_1 = 14 \text{ km s}^{-1}$ . Both transients show vague but recognizable double structure. Their lifetimes are less than 1 minute. Again, all the events shown in Figure 11, as well as an overwhelming majority of transients at any moment of time, belong to the “bow-shock” class. Contrary to this, events that may be classified as true microjets (collimated plasma streaming; cf. Fig. 8) are much more rare. For comparison of their observed signatures, we show one more example seen in the November 20 data set (Fig. 12).

Figure 12 shows snapshots of the upper penumbra at two times, with a  $10.2 \times 15.2 \text{ Mm}^2$  field of view. The white box at UT 12:06:12 demarcates the region with a fast transient that clearly exhibits proper, jetlike motion. A time series of the microjet is shown in the middle row. Its lifetime is a little over 30 s, and velocity exceeds  $50 \text{ km s}^{-1}$ . Its motion is directed *along* its axis, unlike the “transverse” motion of bow-shock-type transients. For comparison, the bottom row shows an example of a “favorably” oriented bow-shock-type transient. Its measured velocity is  $\approx 20 \text{ km s}^{-1}$ , its lifetime is about 2 minutes, and its double structure is clearly visible. The white dotted box in Figure 12 (*top right panel*) and three arrows marked by asterisks are related to Figure 13, which we use to illustrate the model of bow-shock formation. The position of the bow shock is marked by a white dashed arc. It appears around UT 13:29:26 (half an hour earlier than the snapshot shown in Fig. 12). Similar events under less favorable angles, showing only bright arcs, are marked by arrows with a star.

We briefly summarize our observational results as follows:

1. The chromosphere above penumbrae is highly dynamic and shows an abundance of bright, elongated transients at any given moment in time.
2. Transients are always associated with bright points seen in G-band images.
3. Bright points are usually located at the Y-shaped fork made by neighboring penumbral filaments but may be found anywhere in the penumbra.
4. We find two different types of chromospheric transients. One type shows strongly elongated brightenings that move almost perpendicular to their long axes. Their measured velocities range from  $\leq 1.5$  to  $\approx 20 \text{ km s}^{-1}$ . We identify them as bow shocks. The

other type is collimated plasma motion directed along their long axis. We identify them as microjets. Their measured velocities are well above  $20 \text{ km s}^{-1}$ .

5. The bow-shock-type transient makes the vast majority of chromospheric brightenings above the penumbra. Many of them exhibit a double structure.

6. The lifetime of bow shocks ranges from  $\leq 40 \text{ s}$  to  $\geq 6 \text{ minutes}$ . Their apparent length is in between 2000 and 10,000 km, and their width is 300–600 km. The lifetime of microjets is usually  $\leq 1 \text{ minute}$ , and their length is  $\leq 1000 \text{ km}$ .

7. The appearance of bow shocks (from the observer’s point of view), whether or not their double structure is seen, their spatial scale, and measured velocities strongly depend on their location, the position of the sunspot, and the orientation of their trajectory planes with respect to the line of sight.

In the next section we address the phenomenology of post-reconnection processes in penumbral filaments and show that the observed regularities are a natural consequence of these processes.

#### 4. PHENOMENOLOGY AND QUANTITATIVE ANALYSIS

As discussed earlier, the specific character of postreconnection dynamics at the photospheric level is determined basically by finite plasma beta and sharp stratification of the low atmosphere (see Fig. 3). Pressure equilibrium in a high plasma  $\beta$  environment implies that, after reconnection, magnetic field lines remain confined in thin flux tubes. In straightening, the reconnection products create a slingshot effect. At the periphery of a sunspot, flux tubes strongly deviate from the vertical, as does the bisector of their collision angle (Fig. 3b). In this case, the reconnection products acquire U- and  $\cap$ -shaped forms with respect to gravity.

We focus here on further dynamics of the U-shaped reconnection product. In this case, two major forces, the magnetic tension and buoyancy force, both act in the upward direction leading to shock formation. Also, under specific conditions, this leads to the appearance of lateral jets (Tarbell et al. 1999; Ryutova et al. 2003). The process is always accompanied by an enhanced brightening of a small reconnection region.

One more important effect associated with finite plasma  $\beta$  and sharp stratification occurs when a U-shaped postreconnection product straightens and accelerates upward, exceeding the sound speed. In this case, a bow shock is formed in front of the flux tube, as is usual in front of any blunt body moving with supersonic velocities. It is just this macroscopic effect that, we believe, is observed in the form of bright, elongated transients all over penumbrae. The effect is as ubiquitous as the ongoing reconnection processes between penumbral filaments. More importantly, unlike special conditions required for the generation of true plasma jetting (Tarbell et al. 1999; Ryutova et al. 2003), the formation of bow shocks requires only that the flux tube, still having well-defined boundaries, reaches transonic velocities. This simple condition makes bow shocks—bright, elongated transients—appear easily and densely occupy the chromosphere above penumbrae.

Below we detail some basic calculations of the formation of bow shocks and perform quantitative analysis.

##### 4.1. Dynamics of U-shaped Filaments

We follow the energy analysis carried out by Ryutova et al. (2003) and evaluate major forces acting on the U-shaped reconnection product. As mentioned above, magnetic and buoyancy forces act in the same, upward direction accelerating the straightening segment of a flux tube. On the other hand, the flux tube, as a well-defined body moving with velocity  $u$  in the ambient

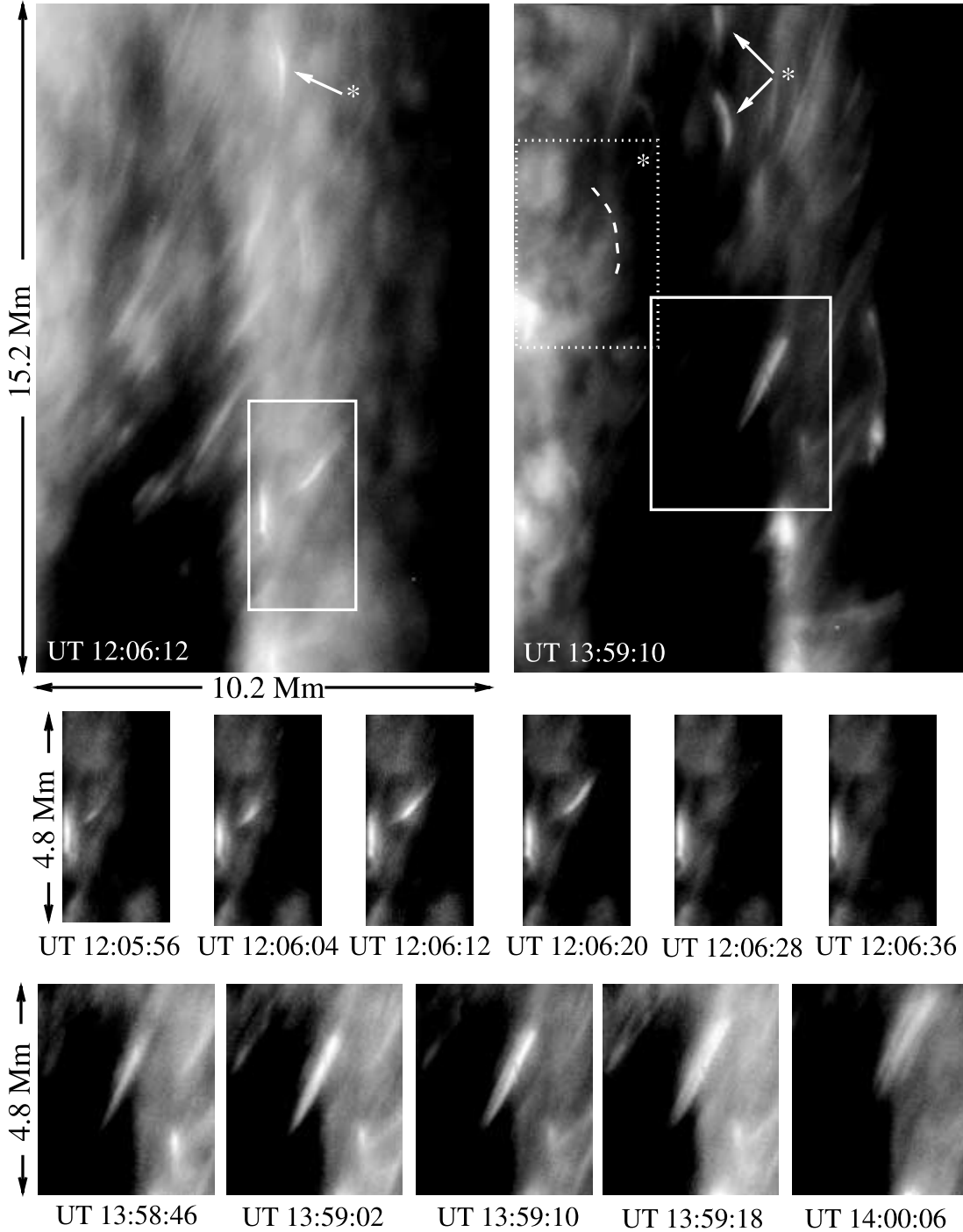


FIG. 12.—Comparison of true microjet and bow shock. *Top*: Snapshots of the upper part of the penumbra at two instances of time. *Middle*: True microjet with a lifetime of about 30 s, traveling in the radial direction with velocity  $\geq 50 \text{ km s}^{-1}$ . *Bottom*: More favorably oriented transient of a bow-shock nature; its measured velocity is  $\approx 20 \text{ km s}^{-1}$ , its lifetime is about 2 minutes, and its double structure is quite visible. The meaning of the dotted box and white arrows marked by asterisks in the top right panel is explained in the text.

plasma, experiences the action of a frictional force,  $F_{\text{drag}} = \frac{1}{2} C_D \rho u^2 S_{\text{srf}}$ , where  $C_D$  is the drag coefficient and  $S_{\text{srf}}$  is the flux tube area transverse to the direction of motion.

It is important that the drag force is negligibly small at large Reynolds numbers (small  $C_D$ ) and small velocities, e.g., in the parameter domain  $\text{Re} \geq 10^3$ ,  $u < c_s$ ,  $C_D \approx 0.1\text{--}0.2$  (see, e.g., Parker 1979). However, when  $u$  exceeds the sound speed,  $c_s$ , the frictional force increases abruptly. At the velocity  $u \approx 1.5 - 2c_s$ ,  $C_D$  becomes of the order of unity (Landau & Lifshitz 1997) and the drag force becomes strong enough to restrict the upward

motion of the flux tube to values not exceeding  $M = u/c_s \approx 1.5\text{--}2.5$ . At the same time, conditions for bow-shock formation are met.

In the following, we adopt for simplicity an isothermal model,  $\rho = \rho_0 \exp(-z/\Lambda)$ , with a constant scale height,  $\Lambda = p/\rho g$ . The subscript “0” refers to the point where reconnection occurred. Consider first a U-shaped flux tube with vertical axis of symmetry as shown in the left panel of Figure 13. The right panel of the figure contains snapshots of Ca II H brightenings, which we believe have a configuration similar to the process shown in the

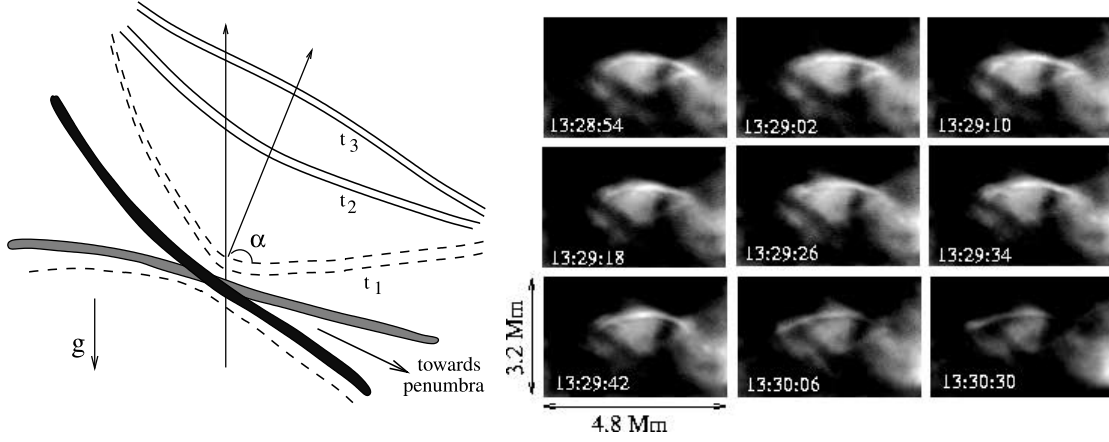


FIG. 13.—Bow-shock formation. *Left*: Sketch of the straightening U-shaped reconnection product with an opening angle  $2\alpha$ . *Right*: Possible observational analogy. The image, rotated by  $90^\circ$ , is located on the side of the penumbra closest to disk center and marked by the dotted box in the top right panel of Fig. 12. Similar events are marked in the same snapshot by white arrows and asterisks.

left panel. We bring the sketch and observations together only for illustrative purposes. It should be noted, however, that such a configuration is seen repeatedly in the observations. Some examples are marked by asterisks in Figure 12; the dashed box in this figure is the area shown in the right panel of Figure 13. The location of the bow shock itself is marked by the dashed arc: at UT 13:59:10 it was already gone. We would like to note, however, that the sketch shown in Figure 13 is simplistic and cannot be understood literally.

At some height  $z$  above the reconnection level, the length of the straightened segment is  $2z \tan \alpha$  (Fig. 13, *left panel*), and its cross section is  $S = S_0 \exp(z/2\Lambda)$ . In what follows, we drop for simplicity the  $\sin \alpha$  correction to height.

The gravitational force over the ascending segment of the flux tube at height  $z$  is

$$F_{\text{gr}} = 2\rho_0 g S_0 z \exp(-z/2\Lambda) \tan \alpha. \quad (2)$$

The change of the gravitational energy at some height  $h$ ,  $\Delta W_{\text{gr}} = -\int_0^h F_{\text{gr}} dz$ , is then

$$\Delta W_{\text{gr}} = \frac{B_0^2}{4\pi} 4\Lambda S_0 \tan \alpha \exp\left(-\frac{h}{2\Lambda}\right) \left[1 + \frac{h}{2\Lambda} - \exp\left(\frac{h}{2\Lambda}\right)\right] < 0. \quad (3)$$

The change of magnetic energy,  $\Delta W_{\text{mag}} \equiv W_{\text{mag}}^h - W_{\text{mag}}^0$  (integrated over the path of the ascending segment), is

$$\Delta W_{\text{mag}} = -\frac{B_0^2}{4\pi} \frac{2\Lambda S_0}{\cos \alpha} \exp\left(-\frac{h}{2\Lambda}\right) \left[\exp\left(\frac{h}{2\Lambda}\right) - 1 - \frac{h}{2\Lambda} \sin \alpha\right] < 0. \quad (4)$$

In addition to the variation of the magnetic energy,  $\Delta W_{\text{mag}}$ , the work,  $p dV$ , makes an equal contribution to the total variation of the potential energy of the system (Ryutova et al. 2003), i.e.,

$$\Delta W_{\text{pot}} = 2\Delta W_{\text{mag}} + \Delta W_{\text{gr}}, \quad (5)$$

or using equations (3) and (4),

$$\Delta W_{\text{pot}} = -\rho_0 v_{A0}^2 \frac{4\Lambda S_0}{\cos \alpha} \exp\left(-\frac{h}{2\Lambda}\right) \times \left\{ (1 + \sin \alpha) \left[ \exp\left(\frac{h}{2\Lambda}\right) - 1 \right] - \left(\frac{h}{\Lambda}\right) \sin \alpha \right\}. \quad (6)$$

Respectively, a total force acting upward on the ascending segment at height  $h$  is

$$F_{\text{up}} = \rho_0 v_{A0}^2 \frac{4\Lambda S_0}{h \cos \alpha} \exp\left(-\frac{h}{2\Lambda}\right) \times \left\{ (1 + \sin \alpha) \left[ \exp\left(\frac{h}{2\Lambda}\right) - 1 \right] - \left(\frac{h}{\Lambda}\right) \sin \alpha \right\}. \quad (7)$$

As already discussed, when the velocity of the ascending flux tube  $u$  exceeds the sound speed, the friction coefficient,  $C_D$ , becomes on the order of unity, and the drag force increases abruptly, restricting the upward motion of the flux tube. As shown in Ryutova et al. (2003), the tip of the straightening segment reaches transonic velocities quite quickly, only in a few scale heights (see Fig. 6). From then on, the motion of the flux tube is determined by the balance of forces acting upward (eq. [7]) and the drag force:

$$F_{\text{drag}} = \frac{1}{2} C_D \rho u^2 S_{\text{srf}}, \quad (8)$$

where  $S_{\text{srf}} = \pi R 2h \tan \alpha = S(2h/R) \tan \alpha$  is the flux tube area transverse to the direction of motion,  $S = \pi R^2$ . With this, the drag force at height  $h$  becomes

$$F_{\text{drag}} = \frac{1}{2} C_D \rho_0 u^2 S_0 \exp\left(-\frac{3h}{4\Lambda}\right) \frac{2h \tan \alpha}{R_0}. \quad (9)$$

From equations (7) and (9), we find the velocity at the tip where these forces are balanced (this implies  $C_D \simeq 1$ ) to be

$$u_f = v_{A0} \left( \frac{4\Lambda R_0 \exp(h/4\Lambda)}{h^2 \sin \alpha} \times \left\{ (1 + \sin \alpha) \left[ \exp\left(\frac{h}{2\Lambda}\right) - 1 \right] - \left(\frac{h}{\Lambda}\right) \sin \alpha \right\} \right)^{1/2}. \quad (10)$$

The height where the bow shock is expected to form corresponds to a final velocity of the flux tube on the order of  $u_f \simeq (1.5-2)c_s$ .

For quantitative estimates, assuming that the reconnection occurs close to the surface, we take  $\rho_0 = 2.25 \times 10^{-7} \text{ g cm}^{-3}$ , scale height  $\Lambda = 150 \text{ km}$ , and sound speed  $c_s = 8 \text{ km s}^{-1}$ . We

TABLE 1  
FINAL VELOCITY OF A SHOCK AT DIFFERENT HEIGHTS AND ANGLES

| PARAMETER                  | $h = 800$ km        |                     |                     | $h = 1000$ km       |                     |                     | $h = 1100$ km       |                     |                     |
|----------------------------|---------------------|---------------------|---------------------|---------------------|---------------------|---------------------|---------------------|---------------------|---------------------|
|                            | $\alpha = 60^\circ$ | $\alpha = 50^\circ$ | $\alpha = 40^\circ$ | $\alpha = 60^\circ$ | $\alpha = 50^\circ$ | $\alpha = 40^\circ$ | $\alpha = 60^\circ$ | $\alpha = 50^\circ$ | $\alpha = 40^\circ$ |
| $M$ .....                  | 1.35                | 1.42                | 1.5                 | 1.9                 | 2                   | 2.1                 | 2.3                 | 2.4                 | 2.5                 |
| $u_f$ (km s $^{-1}$ )..... | 10.8                | 11.36               | 12                  | 15.2                | 16                  | 16.8                | 18.4                | 19.2                | 20                  |

assume a filament radius of  $R_0 = 40$  km. The Alfvén velocity in a magnetic field of  $B = 1000$  G is  $v_A = 6$  km s $^{-1}$ . For these parameters, Table 1 shows estimated heights where the Mach number,  $M = u_f/c_s$ , reaches values of 1.5–2 for different angles of collision and corresponding opening angles  $2\alpha$ .

In the next section we use these parameters for quantitative analysis of bow-shock properties. Before doing this, we first return to the phenomenology of the observed double structure, in particular, to connection between the regular behind shock heating and bow shock. As mentioned earlier, a regular shock produced by a slingshot effect propagates faster than the flux tube and must therefore appear before the straightening flux tube reaches transonic velocities and becomes able to generate a bow shock.

Shocks resulting from photospheric reconnections and their evolution, energy transfer, and release in the chromosphere and transition region have been studied earlier in a series of papers (see, e.g., Tarbell et al. 1999; Ryutova & Tarbell 2000, 2003; Ryutova et al. 2001). It was demonstrated (in both observations and theory) how cancellation of small-scale magnetic elements in the quiet photosphere leads to shock formation and to the eventual appearance of chromosphere/transition region microflares, jets, and their combinations. It is interesting that the evolution of shocks and shock-shock interaction was directly observed (Ryutova & Tarbell 2000, 2003).

Ryutova et al. (2001) studied photospheric reconnections and shock formation in various magnetic and nonmagnetic environments and calculated corresponding heights of shock formation and shock velocities. We use their results here for the Alfvén/MHD branch (Fig. 2, case 3 in Ryutova et al. 2001) to compare the shock velocity with the velocity of the ascending flux tube, equation (10). Solution of equation (16) of Ryutova et al. 2001 (see also their Fig. 4b) has a form

$$u_{sh}(z) = v_{A0} \frac{\sqrt{(3z_0/\Lambda) \exp(z/2\Lambda) [1 - \exp(-3z/4\Lambda) - 3z_0/4\Lambda]}}{1 - \exp(-3z/4\Lambda)}, \quad (11)$$

where  $z_0$  is the height of shock formation in a homogeneous atmosphere:

$$z_0 = \frac{2}{\gamma + 1} \frac{c_{s0}^2}{v_{A0}^2} R. \quad (12)$$

Plots of  $u_{sh}$  and  $u_f$  (eq. [10]) for three opening angles are shown in Figure 14. We use the same parameters as those used above for construction of Table 1.

One can see that the regular shock reaches the transonic region earlier than the bow shock (note that for chosen parameters,  $c_s = 8$  km s $^{-1}$ ,  $v_{A0} = 6$  km s $^{-1}$ , Mach one,  $M = u/c_s = 1$ , corresponds to  $u/v_{A0} = 1.5$  in Fig. 14).

To estimate times needed for regular shocks and bow shocks to reach approximately the same height, we need to integrate equations (10) and (11), i.e., evaluate the integral  $t = \int_a^b dz/u(z)$ .

Vertical dashed lines in Figure 14 intersecting the plots mark end points for numerical integration. We choose for the lower limit of integrals  $a_1 = 0.5$ , i.e.,  $z \simeq 75$  km (half of the scale length,  $\Lambda$ ) above the reconnection point. The value  $b_1 = 1.1$  corresponds to the height of a regular shock formation,  $M = 1$  ( $u/v_{A0} = 1.5$ ). Corresponding heights for bow shocks are  $c_1 = 4$  at  $\alpha = 40^\circ$  and  $d_1 = 4.55$  at  $\alpha = 60^\circ$ . Numerical integration of  $u_{sh}$  (eq. [11]) between  $a_1$  and  $b_1$ , gives a time of  $t_{b1} = 16.5$  s. Numerical integration of  $u_f$  (eq. [10]) with end points  $a_1 = 0.5$  and  $c_1 = 4$ ,  $a_1 = 0.5$  and  $d_1 = 4.55$  gives the estimates of time when the velocity of the ascending portion of the flux tubes reaches  $M = 1$ :  $t_{c1} = 65.5$  s ( $\alpha = 40^\circ$ ),  $t_{d1} = 74$  s ( $\alpha = 60^\circ$ ). These estimates show that there is a finite time interval,  $\Delta t$ , between the appearance of a regular shock and following bow shock. Thus, for  $M = 1$ ,  $\Delta t = 49$  s ( $\alpha = 40^\circ$ ) and  $\Delta t = 57.5$  s ( $\alpha = 60^\circ$ ).

For higher Mach numbers, the “delay time” slightly drops. A similar procedure for  $M = 1.5$  ( $u/v_{A0} = 2$ ) gives the following estimates. The regular shock reaches this level in  $t_{b2} = 39$  s. The flux tube reaches this velocity in  $t_{c2} = 83.5$  s for  $\alpha = 40^\circ$  and in  $t_{d2} = 88.7$  s for  $\alpha = 60^\circ$ . Delay times are  $\Delta t = 44.5$  and  $49.7$  s, respectively.

The observed time delay for the appearance of a bow shock ranges from tens of seconds to minutes. For the examples given in this paper, we have the following numbers. The bow shock shown in Figure 6 appears in 29 s after a regular behind shock heating. The time delay, in the case of the bow shock shown in Figure 7, is about 1 minute. In the case shown in Figure 10, the time delay is 48 s. In the example shown in Figure 11b, the bow shock appears in about 40 s, and in the last example (Fig. 12, bottom row), the time delay is only 24 s. Thus, the observed and estimated time delays are in quite good agreement.

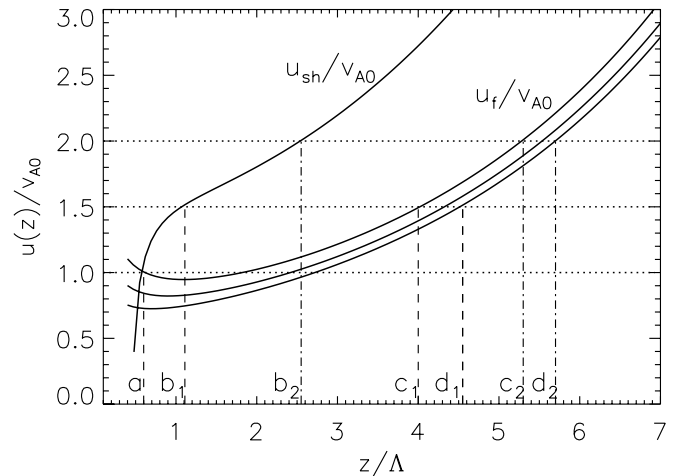


FIG. 14.—Shock amplitudes as a function of height: the upper curve, marked as  $u_{sh}/v_{A0}$ , corresponds to the shock resulting from postreconnection slingshot (Ryutova et al. 2001). Three lower curves, marked as  $u_f/v_{A0}$ , correspond to the velocity of the ascending flux tube for three opening angles,  $40^\circ$ ,  $50^\circ$ , and  $60^\circ$  (top to bottom). For the meaning of dashed lines and letter marks see the text.

TABLE 2  
CALCULATED BOW SHOCK PARAMETERS

| PARAMETER                             | $h = 800$ km        |                     |                     | $h = 1000$ km       |                     |                     | $h = 1100$ km       |                     |                     |
|---------------------------------------|---------------------|---------------------|---------------------|---------------------|---------------------|---------------------|---------------------|---------------------|---------------------|
|                                       | $\alpha = 60^\circ$ | $\alpha = 50^\circ$ | $\alpha = 40^\circ$ | $\alpha = 60^\circ$ | $\alpha = 50^\circ$ | $\alpha = 40^\circ$ | $\alpha = 60^\circ$ | $\alpha = 50^\circ$ | $\alpha = 40^\circ$ |
| $M$ .....                             | 1.35                | 1.42                | 1.5                 | 1.9                 | 2                   | 2.1                 | 2.3                 | 2.4                 | 2.5                 |
| $\epsilon$ .....                      | 0.662               | 0.622               | 0.583               | 0.458               | 0.437               | 0.420               | 0.392               | 0.380               | 0.370               |
| $\Delta$ (km).....                    | 370                 | 379                 | 386                 | 489                 | 487                 | 485                 | 528                 | 525                 | 522                 |
| $h_{\text{bow}}$ (km).....            | 1170                | 1179                | 1186                | 1489                | 1487                | 1485                | 1628                | 1625                | 1621                |
| $L_{\text{bow}}$ (km).....            | 2770                | 1910                | 1343                | 3464                | 2384                | 1678                | 3810                | 2622                | 1846                |
| $T_1$ (K).....                        | 9645                | 10000               | 10500               | 13200               | 14000               | 15000               | 16600               | 17500               | 18500               |
| $T_2$ (K).....                        | 12900               | 14100               | 15700               | 25800               | 29000               | 33000               | 41300               | 46200               | 51600               |
| $u_{\text{bow}}$ (km s $^{-1}$ )..... | 10.8                | 11.36               | 12                  | 15.2                | 16                  | 16.8                | 18.4                | 19.2                | 20                  |

#### 4.2. Bow Shock

Formation of bow (*detached*) shocks in front of accelerating flux tubes is a natural occurrence, as for any blunt body moving with supersonic velocities. This condition is met in many environments, including those surrounding aircraft and space objects. Parameters of bow shocks are determined by Mach number and pressure  $p$ , density  $\rho$ , and temperature  $t$  relations across the shock (Landau & Lifshitz 1997):

$$\frac{p_2}{p_1} = \frac{2\gamma M^2 - (\gamma - 1)}{\gamma + 1}, \quad \frac{\rho_2}{\rho_1} = \frac{(\gamma + 1)M^2}{2 + (\gamma - 1)M^2}, \quad (13)$$

$$v_2 = v_1 \frac{2 + (\gamma - 1)M^2}{(\gamma + 1)M^2}, \quad (14)$$

$$T_2 = T_1 \frac{[2\gamma M^2 - (\gamma - 1)][2 + (\gamma - 1)M^2]}{(\gamma + 1)^2 M^2}. \quad (15)$$

The subscript “2” refers to the region behind the bow shock and the subscript “1” denotes parameters of the incident stream associated with the flux tube;  $\gamma$  is a specific heat ratio. These are determined by the standard expressions for the variation of quantities along the streamline (Landau & Lifshitz 1997, p. 323), e.g.,  $T_1 = T_0[1 + \frac{1}{2}(\gamma - 1)M^2]$ . A standoff distance of the bow shock,  $\Delta$  (distance between the bow shock and the body creating it), is known to be proportional to the inverse density ratio across the shock,  $\Delta \sim h(\rho_1/\rho_2)$ :

$$\frac{\Delta}{h} = \zeta \frac{2 + (\gamma - 1)M^2}{(\gamma + 1)M^2}. \quad (16)$$

The coefficient of proportionality,  $\zeta$ , is usually of the order of unity. For cylindrical objects it can be approximated as (see, e.g., Hayes & Probstein 1966)

$$\zeta = \ln \frac{4}{3\epsilon}, \quad \epsilon = \frac{2 + (\gamma - 1)M^2}{(\gamma + 1)M^2}. \quad (17)$$

With equations (13)–(17) one can estimate the position of the bow shock,  $h_{\text{bow}} = h + \Delta$ , temperature, and velocity. In addition, given that the lateral extension of the bow shock is of the same order of magnitude as the straightened segment of the flux tube, the “length” of the bow shock,  $L_{\text{bow}}$ , can be estimated as  $2h \tan \alpha$ , and its thickness should be on the order of the standoff distance,  $d_{\text{bow}} \simeq \Delta$ . In Table 2 we estimate bow-shock parameters at different Mach numbers for three different angles.

In principle, most of the transient parameters are observable. The observed length of transients (ranging from 2000 to 10,000 km),

their width (300–600 km), and their lifetime are in good order-of-magnitude agreement with the calculated quantities given in Table 2. The uncertainty in measuring velocities and linear scales of transients is largely due to the uncertainty of their true orientation with respect to the line of sight. This is illustrated in Figure 14.

When two neighboring filaments in penumbrae reconnect, the upper, U-shaped reconnection product is accelerated and eventually generates a bow shock. The reconnection region may have arbitrary orientation with respect to the observer depending on the heliographic location of the sunspot and the azimuthal location of the reconnecting filaments in the penumbra. The orientation and location of the penumbral bisector are essential as well. If the final orientation of the plane in which the bow shock moves is similar to plane “1” in Figure 14, i.e., if the line of sight lies almost in the same plane, the transient will appear almost motionless, as is often seen in observations. With arbitrary angle  $\theta$ , the velocity of the transient from the observer’s point view

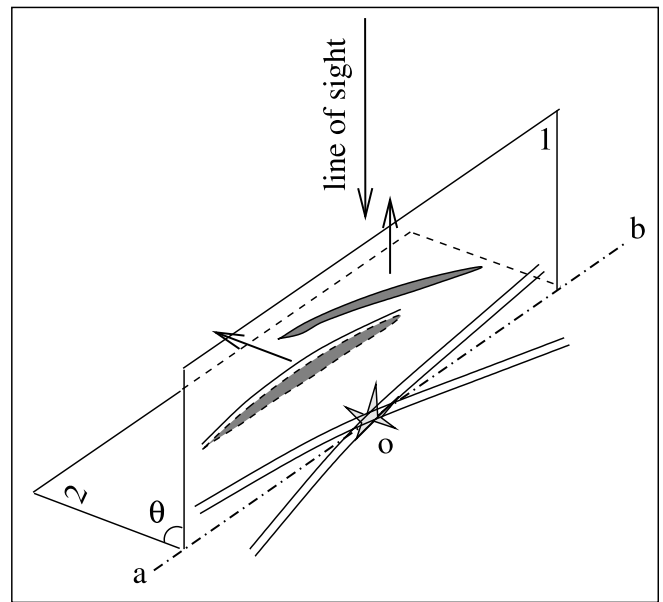


FIG. 15.—Orientation of the plane in which the bow shock travels depends on the orientation of the upper postreconnection flux tube producing a slingshot effect and may be arbitrary. This in turn determines the appearance, velocity, and dimensions of the bow shock from the observer’s point of view. Point “o” is a reconnection region, while “ab” is the bisector of a collision angle between interacting penumbral filaments. If the plane is in position 1, the transient appears as a single elongated brightening, but, with increasing angle  $\theta$ , the double structure of the transient becomes visible.

TABLE 3  
THERMAL ENERGY AT DIFFERENT HEIGHTS AND ANGLES

| PARAMETER                                       | $h = 800$ km        |                     |                     | $h = 1000$ km       |                     |                     | $h = 1100$ km       |                     |                     |
|---|---------------------|---------------------|---------------------|---------------------|---------------------|---------------------|---------------------|---------------------|---------------------|
|   | $\alpha = 60^\circ$ | $\alpha = 50^\circ$ | $\alpha = 40^\circ$ | $\alpha = 60^\circ$ | $\alpha = 50^\circ$ | $\alpha = 40^\circ$ | $\alpha = 60^\circ$ | $\alpha = 50^\circ$ | $\alpha = 40^\circ$ |
| $M = u_{\text{bow}}/c_s$ .....                  | 1.35                | 1.42                | 1.5                 | 1.9                 | 2                   | 2.1                 | 2.3                 | 2.4                 | 2.5                 |
| $W_{\text{therm}} (10^{26} \text{ ergs})$ ..... | 5.5                 | 6.0                 | 6.13                | 4.12                | 4.48                | 4.56                | 3.26                | 3.53                | 3.57                |

may range from almost zero to its maximum value. In our data sets (showing the sunspot traveling from limb to limb) the maximum measured velocities, perpendicular to the transient long axis, are found to be  $19\text{--}20 \text{ km s}^{-1}$ . Calculated velocities show a strong dependence on height of the transient formation and range from  $11$  to  $20 \text{ km s}^{-1}$ . Along the direction of motion, the appearance of the transient is also affected by its orientation. When the line of sight is parallel to the plane of transient motion ( $\theta = 90^\circ$ ), the transient appears as a single elongated brightening. With a finite angle  $\theta$ , the double structure of the transient becomes visible and may appear to be moving either away from or toward the observer. Possible orientation of the plane in which the bow shock travels is shown in Figure 15.

One of the most accurate parameters for comparison is, in fact, the lifetime of transients. The observed lifetimes range from tens of seconds to 2–6 minutes.

For theoretical estimates of the lifetime, we restrict ourselves by considering shock-related dissipation. First, we find the released thermal energy, and then the corresponding dissipation rate. This is done in the next section.

#### 4.3. Energy Release and Lifetime of Brightening

Energy release during the final stage of the straightening flux tube, when its velocity reaches  $u_f$ , can be estimated from the difference between the potential energy (eq. [6]) and the kinetic energy of the flux tube at the corresponding height  $h$  (cf. Ryutova et al. 2003):

$$\Delta W_{\text{therm}} = -\Delta W_{\text{pot}} - \frac{\rho_0 u_f^2}{2} 2h \tan \alpha S_0 \exp\left(-\frac{h}{2\Lambda}\right). \quad (18)$$

Using equations (6) and (10), one obtains

$$\Delta W_{\text{therm}} = \rho_0 v_{A0}^2 \frac{4\Lambda S_0}{\cos \alpha} \exp\left(-\frac{h}{2\Lambda}\right) \times \left\{ (1 + \sin \alpha) \left[ \exp\left(\frac{h}{2\Lambda}\right) - 1 \right] - \frac{h}{\Lambda} \sin \alpha \right\} \delta, \quad (19)$$

where

$$\delta = \left[ 1 - \frac{R_0}{h} \exp\left(\frac{h}{4\Lambda}\right) \right]. \quad (20)$$

Using the same parameters as above ( $\rho_0 = 2.25 \times 10^{-7} \text{ g cm}^{-3}$ ,  $\Lambda = 150 \text{ km}$ ,  $R_0 = 40 \text{ km}$ ,  $v_A = 6 \text{ km s}^{-1}$ ) for the chosen heights (or, equivalently, Mach numbers) and angles (eq. [19]), one obtains the estimates for thermal energy shown in Table 3.

One can see that the released energy is in the range of  $(3\text{--}6) \times 10^{26} \text{ ergs}$ . This is comparable with the energy of blinkers, micro-

flares, and other short-lived transients observed in the chromosphere/transition region.

To calculate the lifetimes of transients/bow shocks, we recall the fact that the strength of a weak shock and its energy,  $E(t)$ , are known to diminish as  $1/t^2$  (Landau & Lifshitz 1997), namely,

$$E(t) = \frac{E_0}{(1 + \alpha_n u t / h)^2}, \quad (21)$$

where  $\alpha_n = \frac{1}{2}(\gamma + 1)$  is a coefficient of nonlinearity for a polytropic gas,  $\alpha_n = 4/3$ . Plots of  $E(t)$  normalized by the initial energy carried by a shock are shown in Figure 16. For illustrative purposes, we use an example with  $\alpha = 50^\circ$ . The solid line corresponds to a bow shock at  $h = 1179 \text{ km}$ , velocity  $u_{\text{bow}} = 11.36 \text{ km s}^{-1}$ , and temperature  $T = 1.4 \times 10^4 \text{ K}$ . The dashed line corresponds to  $h = 1487 \text{ km}$ ,  $u_{\text{bow}} = 16 \text{ km s}^{-1}$ , and  $T = 2.9 \times 10^4 \text{ K}$ . The dot-dashed line corresponds to  $h = 1625 \text{ km}$ , velocity  $u_{\text{bow}} = 19.2 \text{ km s}^{-1}$ , and  $T = 4.6 \times 10^4 \text{ K}$ . The characteristic time in which the energy of the bow shock drops by a factor of  $e = 2.7$  is in the range of 40–50 s. For the chosen example, the average thermal energy is  $W_{\text{therm}} = 4 \times 10^{26} \text{ ergs}$ , which drops to  $\simeq 1.5 \times 10^{26} \text{ ergs}$  in about 1 minute. A more significant, order-of-magnitude decay occurs in 130–180 s. Thus, roughly, the lifetime of the bow shock/transients may be from 40 s to 3 minutes. This is the time interval corresponding to the observed lifetimes of transient brightenings.

#### 5. SUMMARY

Observations of sunspot penumbrae obtained with the SOT instrument on *Hinode* in 4305 Å G band and Ca II 8500 Å H line reveal an abundant population of highly dynamic transient phenomena in the overlying chromosphere and show clear regularities

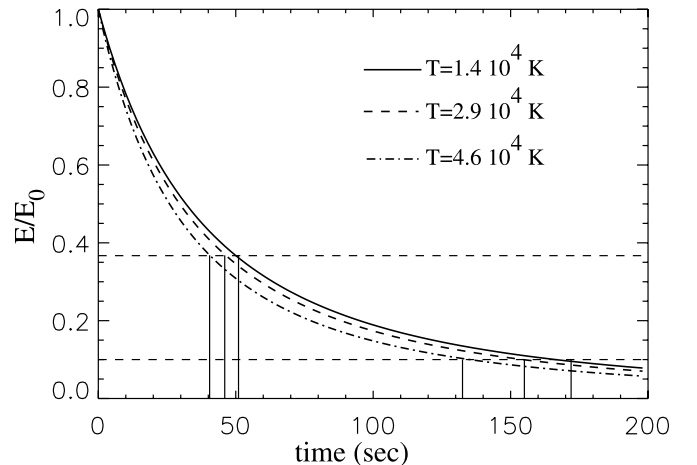


FIG. 16.—Decay of the bow-shock energy. Characteristic lifetimes range from 40 s to 3 minutes.

in their properties. New details in chromospheric dynamics were obtained thanks to observations of the sunspot at different locations during its passage from the east to west limb, showing the penumbra at various angles.

We found two different classes of bright elongated transients. The first discriminator that stands out is a difference in the *direction* of their motion with respect to their long axes.

One class includes the transients that move as a whole in a direction almost perpendicular to their long axes. We classify these as bow shocks. These types of transients make up the vast majority of all observed transients.

Their measured velocities range from  $\leq 1.5$  to  $\sim 20$  km s<sup>-1</sup>. As the orientation of the plane of the transient motion may be arbitrary, measured velocities may range from almost zero (when the plane of transient motion is parallel to the line of sight) to their maximum values (when the plane of transient motion is normal to the line of sight). This explains a wide range of velocities in our data sets measured when the sunspot was in various locations on the disk.

A remarkable new property revealed in these observations is that many of the bow-shock-type transients exhibit a double structure. It usually develops soon after the appearance of the “first light” at a characteristic standoff distance from it. The double system then travels as a whole until it starts to dissipate. This feature strongly supports the bow-shock nature of transients. The fact that not all the transients show a double structure is, like apparent velocities, affected by the orientation of the plane of the transient motion with respect to the line of sight.

Lifetimes of bow-shock-type transients range from  $\leq 40$  s to  $\geq 6$  minutes. Their apparent length is between 2000 and 10,000 km and their width is 300–600 km. In double structures, the standoff distance is on the order of, or less than, the width of the “secondary” transient (the bow shock itself).

The other type, representing the minority of chromospheric transients, may be classified as microjets. They have properties of collimated plasma streaming directed *along* their axes in the radial direction.

Their measured velocities (in our data sets) range from 20 to 50 km s<sup>-1</sup>. Lifetimes of microjets are  $\leq 1$  minute. Their apparent length hardly exceeds 1000 km. As already mentioned, the number of microjets is significantly less than the ubiquitous bow-shock-type transients covering the entire penumbra at any instance of time.

We find that the observed properties of chromospheric transients can be well understood in the framework of our recent penumbral model (Ryutova et al. 2008). This model is based on the filamentary structure of sunspots where the most natural processes are the ongoing reconnection processes among interlaced filaments. The specific character of photospheric reconnection and postreconnection processes (provided by high plasma  $\beta$  and strong stratification of the low atmosphere) leads to macroscopic effects that are consistent with all observed properties of individual filaments and explains the very formation of penumbrae.

The model also adequately explains the response of the overlying chromosphere to penumbral dynamics, in particular to reconnection and postreconnection processes that take place continually in the underlying penumbra.

The most important effects produced by reconnecting filaments are shocks resulting from a slingshot effect associated with the straightening U-shaped reconnection product. Besides, under the action of magnetic tension and a buoyancy force acting in the same upward direction, a U-shaped flux tube itself quickly accelerates. At transonic velocities in front of it a bow (*detached*)

shock is formed as it usually occurs in cases of blunt bodies moving with supersonic velocities. When the flux tube reaches Mach numbers  $\approx 1.5$ –2, the drag force becomes strong enough to restrict further acceleration of the flux tube. Thus, the bow shock, once formed, tends to remain at the initial standoff distance until the whole system starts to dissipate. The calculated thermal energy of bow shocks and their lifetimes, spatial scales, and velocities are in good agreement with the measured quantities.

Qualitatively, all the observed regularities are fully consistent with the model. This includes, e.g., the elongated shape of chromospheric transients often showing a double structure and moving in a direction perpendicular to their long axes. Transients are always associated with penumbral bright points usually located at Y-shaped forks (reconnection regions), made by neighboring filaments.

The entire process (formation of the Y-shaped fork in the penumbra, local brightening of a reconnection region, appearance of an elongated transient above it) may occur in any place at any given moment of time. It is important that only a limited portion of penumbral filaments participate in each elemental reconnection. The maximum radius, determined by the magnetic Reynolds number, is about  $R_{\max} \sim 36$ –70 km. This means that filaments with radii as small as 150–200 km are subject to multiple reconnections. Therefore, the appearance of bright transients is a recurrent process and is as ubiquitous as interacting penumbral filaments all over penumbrae.

In conclusion, we would like to note that reconnection processes not only affect the dynamics of penumbral filaments but, in the first place, play an important role in fine structure and properties of individual filaments. As shown in Ryutova et al. (2008), each elemental act of reconnection facilitates the onset of a screw pinch instability in reconnected flux tubes, which in turn determines the distribution of electric currents, helical magnetic fields, and temperature inside the filaments. The spectropolarimeter (SP) that operates in synchronous mode with the SOT filtergraph on *Hinode* provides a unique opportunity to study distribution of electric currents in filaments before and after their interaction. Evolution of electric currents is naturally accompanied by evolution of plasma flows inside and outside filaments (Ryutova et al. 1996). The SP spectra taken along the individual filaments and across the Y-shaped configuration in various points will reveal changes in vector magnetic fields, currents, and plasma flows. These changes may provide valuable information on sunspot properties, its energy content, and decay and will also shed light on the origin and a complex nature of Evershed flows.

We thank Dick Shine for help and Ted Tarbell for useful discussions. We also thank the SOT team for making the observations possible. We are grateful to an anonymous referee for many helpful comments and suggestions. This work was performed under the auspices of the US DOE by UC, Lawrence Livermore National Laboratory under contract W-7405-Eng-48 and supported by NASA contract at Stanford and Lockheed Martin (NAG5-10483, MDI). T. E. B. gratefully acknowledges the support of NASA contract NN07AA01C at LMSAL. *Hinode* is a Japanese mission developed and launched by ISAS/JAXA, with NAOJ as domestic partner and NASA and STFC (UK) as international partners. Science operation of *Hinode* is conducted by the *Hinode* science team organized at ISAS/JAXA.



## REFERENCES

- Bellot Rubio, L., Balthasar, H., & Collados, M. 2004, *A&A*, 427, 319  
Bellot Rubio, L., Langhans, K., & Schlichenmaier, R. 2005, *A&A*, 443, L7  
Bellot Rubio, L. R., et al. 2007, *ApJ*, 668, L91  
Berger, T., et al. 2004, *A&A*, 428, 613  
Borrero, J. M., Lites, B. W., & Solanki, S. K. 2008, *A&A*, 481, L13  
Borrero, J. M., Solanki, S. K., Bellot Rubio, L. R., Lagg, A., & Mathew, S. K. 2004, *A&A*, 422, 1093  
Hayes, W. D., & Probst, R. F. 1966, *Hypersonic Flow Theory* (New York: Academic)  
Katsukawa, Y., et al. 2007, *Science*, 318, 1594  
Landau, L. D., & Lifshitz, E. M. 1997, *Fluid Mechanics* (Oxford: Pergamon)  
Langhans, K., et al. 2005, *A&A*, 436, 1087  
Livingston, W. 1991, *Nature*, 350, 45  
Papathanasoglou, D. 1971, *Sol. Phys.*, 21, 113  
Parker, E. N. 1979, *Cosmical Magnetic Fields* (Oxford: Clarendon)  
Petschek, H. E. 1964, *NASA Spec. Pub. SP-50*, 425  
Roupe van der Voort, L. H. M., et al. 2004, *A&A*, 414, 717  
Ryutova, M., Berger, T., & Title, A. 2008, *ApJ*, 676, 1356  
Ryutova, M., Habbal, S., Woo, R., & Tarbell, T. 2001, *Sol. Phys.*, 200, 213  
Ryutova, M., & Tarbell, T. 2003, *Phys. Rev. Lett.*, 90, 191101  
Ryutova, M., Tarbell, T. D., & Shine, R. 2003, *Sol. Phys.*, 213, 231  
Ryutova, M. P., Kaisig, M., & Tajima, T. 1996, *ApJ*, 459, 744  
Ryutova, M. P., & Tarbell, T. 2000, *ApJ*, 541, L29  
Scharmer, G., et al. 2002, *Nature*, 420, 151  
Sütterlin, P., et al. 2004, *A&A*, 424, 1049  
Tarbell, T., Ryutova, M., Covington, J., & Fludra, A. 1999, *ApJ*, 514, L47  
Tarbell, T., Ryutova, M., & Shine, R. 2000, *Sol. Phys.*, 193, 195  
van Noort, M. J., & Roupe van der Voort, L. H. M. 2008, *A&A*, 489, 429